


Article

A DFT Study on Adsorption of SF₆ Decomposition Products on Zr-MOF-808

Tianxiang Lei ^{1,2} , Fangcheng Lv ^{1,2,*} and Bowen Jiang ^{1,2}

¹ State Key Laboratory of Alternate Electrical Power System with Renewable Energy Sources, North China Electric Power University, Baoding 071003, China; narrosn@126.com (T.L.); qq953501277@icloud.com (B.J.)

² Hebei Provincial Key Laboratory of Power Transmission Equipment Security Defence, North China Electric Power University, Baoding 071003, China

* Correspondence: lfc@ncepu.edu.cn

Abstract: Identifying the main byproducts of SF₆ decomposition proves to be an effective strategy for determining the nature and severity of internal discharge faults in gas-insulated switchgears (GISs). In this research, it was suggested to utilize the coordination polymer Zr-MOF-808 as a sensor for the main byproducts of SF₆ decomposition. This study examined the adsorption of SF₆ and its main decomposition products (CF₄, CS₂, SO₂, SO₂F₂, and SOF₂) on Zr-MOF-808, utilizing Gaussian16 simulation software through a method anchored on quantum chemistry. Adsorption parameters were calculated and analyzed, including binding energy, charge transfer, adsorption distance, along with variations in bond length, bond angle, density of states, and frontier orbital of gas molecules. Our research indicated that the Zr-MOF-808 cluster demonstrated varying degrees of chemical adsorption for the six gases, leading to differential conductivity changes in each system following adsorption. Consequently, the detection of resistance value alterations in the materials would allow for the identification of the gas products.

Keywords: SF₆ decomposition products; MOFs; gas sensing materials; quantum chemistry



Citation: Lei, T.; Lv, F.; Jiang, B. A DFT Study on Adsorption of SF₆ Decomposition Products on Zr-MOF-808. *Chemosensors* **2023**, *11*, 402. <https://doi.org/10.3390/chemosensors11070402>

Academic Editor: Eleonora Alfinito

Received: 6 June 2023

Revised: 7 July 2023

Accepted: 15 July 2023

Published: 18 July 2023



Copyright: © 2023 by the authors. Licensee MDPI, Basel, Switzerland. This article is an open access article distributed under the terms and conditions of the Creative Commons Attribution (CC BY) license (<https://creativecommons.org/licenses/by/4.0/>).

1. Introduction

Metal–organic frameworks (MOFs), a novel class of coordination polymer materials, have seen extensive research over the past twenty years since their initial conceptual introduction [1–4]. They have emerged as excellent foundations for a variety of high-performing materials and applications [5–8]. The unique structures and properties of MOFs derive from the versatility in their design [9,10], their structural diversity and malleability [11–13], their customizable pore size, and their high specific surface area and pore volume [14,15]. These characteristics render them significant for applications in gas storage and separation, catalysis, energy storage for batteries, bio-medicine, among others [16–23]. Typically, MOFs' distinctive properties show promise for addressing industrial application challenges such as CO₂ capture, flue gas scrubbing, and enhancing natural gas (NG) and refinery off-gas (ROG) [24–28]. Nevertheless, limited research exists on the use of MOFs in power systems, particularly concerning the adsorption behavior of SF₆ decomposition products like CF₄, CS₂, SO₂, SOF₂, SO₂F₂, and other gases, on MOFs materials.

SF₆ gas finds extensive use as an arc-quenching medium in GISs. Unforeseen internal malfunctions in GISs usually stem from insulation defects, with early insulation failures potentially leading to partial discharges (PDs). During the operation of the equipment, these faults could instigate the decomposition of SF₆ into lower fluorine sulfides (SF_n, *n* = 1–5) [29–31]. Given the presence of minute amounts of O₂ and H₂O, these lower fluorine sulfides could further react to yield SO₂, SOF₂, SO₂F₂, and other primary products [32–34]. Should surface discharges occur in the basin insulator, SF_n might produce CF₄, CS₂, and the like [35,36]. As such, detecting the types and concentrations of discharged SF₆

decomposition products becomes critical for an early identification of equipment fault types and for a prompt evaluation of the GISs' insulation level and operational status [37–39].

Gas sensors serve as efficient instruments for detecting SF₆ decomposition products. Gas-sensitive materials, forming the core of this method, have garnered considerable interest from researchers over the past two decades. A study conducted by Yang, A. et al. revealed that infusing different noble metals into CeO₂ nanoparticles can be an effective approach for engineering high-performance gas sensors for identifying SF₆ decomposition products [40]. Research by Wang, Y. et al. demonstrated that the (101) polyhedron of the metal oxide TiO₂, when altered with Pt(III), significantly enhanced the adsorption of SO₂, SO₂F₂ and SOF₂ [41]. Investigating the modification of the metal sulfide MoS₂, Liu, H. et al. performed a comprehensive study on the adsorption properties and sensing behavior of an Ir-modified MoS₂ monolayer for H₂S, SO₂, and SO₂F₂ using Density Functional Theory (DFT) [42]. Wang, X. et al. discovered that a Rh-doped HfSe₂ monolayer exhibited good adsorption performance for SO₂ gas [43]. Chen, D. et al. confirmed that graphene doped with different elements displayed effective adsorption performance for SF₆ decomposition component gases [44,45]. Despite the impressive gas-sensing properties of these modified nanomaterials, the design and flexibility of inorganic materials are somewhat restricted, thereby limiting their potential for further development. As a novel category of coordination polymer, MOFs materials, thanks to their superior properties, are anticipated to offset the deficiencies of the aforementioned materials.

Zr-MOF-808, a novel coordination polymer material, employs Zr⁴⁺ as the central ion and 1,3,5-tribenzoic acid as the ligand. A detailed investigation conducted by Furukawa, H. et al. elaborated on the preparation methodology and structural analysis of Zr-MOF-808. Their research demonstrated that acid radical ions coordinated with Zr atoms, presenting themselves in an unordered manner as monodentate and bidentate ligands. Zr-MOF-808 exhibits a 6,3-connected three-dimensional structure, forming a tetrahedral cage with an interior pore size of 0.48 nm (Figure 1a). The unique design of these tetrahedral cages allows Zr-MOF-808 to establish a large adamantane cage, having an internal pore size of 1.84 nm (Figure 1b) via vertex sharing [46]. Its crystal structure is presently documented in the Cambridge structure database (DOI: 10.5517/cc12nc8c). A review of the crystal structure information file (CIF) in CCDC1002672 determined that the metal ion/ligand ratio in a Zr-MOF-808 unit cell stands at 39:8.

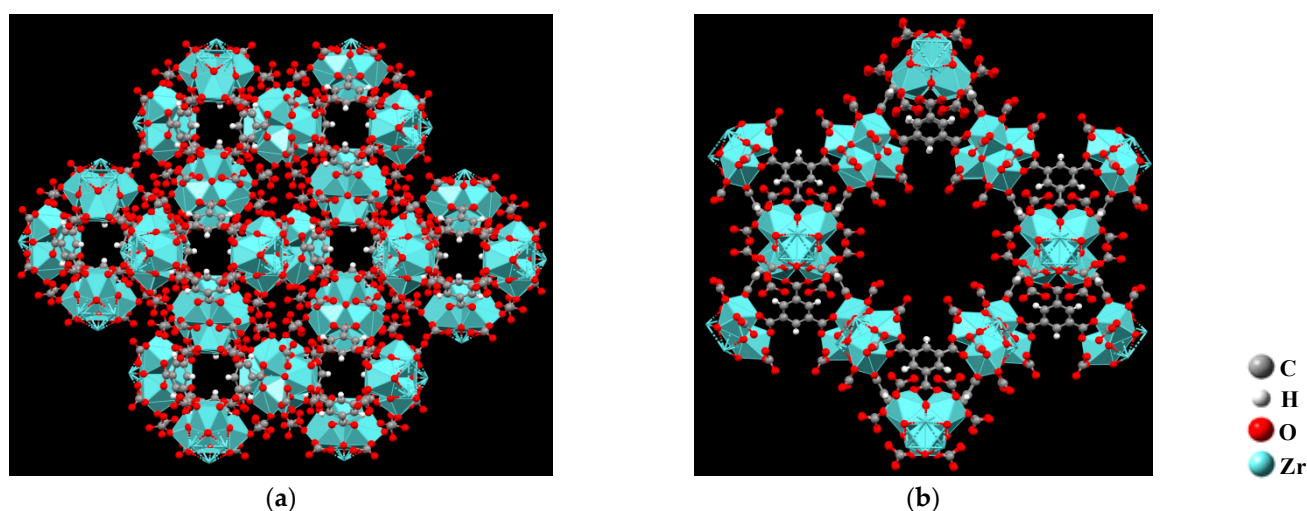


Figure 1. Two pore sizes of Zr-MOF-808: (a) 0.48 nm; (b) 1.84 nm.

As this is a gas-sensing material, its crisscross pore structure with pore sizes of 0.48 nm and 1.84 nm creates a structural basis for the entry of six gas molecules—SF₆, CF₄, CS₂, SO₂, SO₂F₂, and SOF₂—into the pores of the material (Figure 2). In these pores, the unsaturated coordination transition metal Zr⁴⁺ allows gas adsorption. This study explored the applica-

tion of MOFs materials from a new perspective. For the first time, the coordination polymer Zr-MOF-808 was used as a gas-sensing material. The adsorption behaviors of discharged SF₆ decomposition products on this material were studied and analyzed with a simulation method based on the principles of quantum chemistry. The application prospects of Zr-MOF-808 as an online gas-sensitive material for detecting SF₆ decomposition products were theoretically predicted, which provided new ideas for research on the engineering applications of MOFs materials.

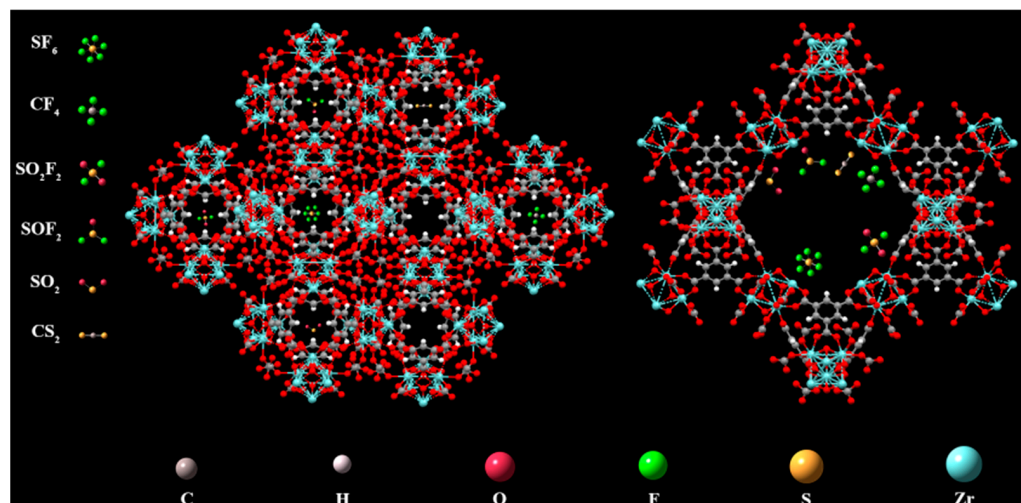


Figure 2. Adsorption simulation of six gases in Zr-MOF-808 pores.

2. Calculation Methods

The modeling involved in this study was completed in the GaussView software, and the structural optimization and single-point adsorption calculation were performed with the Gaussian 16 software. In the application of Gaussian series in quantum chemistry simulation software, Sciortino, G. et al. found that PBE0 had a higher accuracy than those of B3LYP, BP86, and other functionals in the calculation of Ni (II) complexes. Def2-tzvp performed better than the LANL2DZ basis set [47]. The research on Debeffe conducted by L.M. et al. showed that a combination of the PBE0 functional and def-tzvp performed best in the geometric optimization of mononuclear platinum complexes based on the DFT principle. In this study, we use the same exchange-correlation functional, basis set, and van der Waals action correction algorithm as in our previous research study [48]. We set the charge to 0 and the spin multiplicity to 1.

According to the .cif file in CCDC, there are 3800 atoms, 6272 chemical bonds, and 96 polyhedrons in each periodic structural unit of Zr-MOF-808. In order to simplify the calculation, Cluster 1 (Figure 3a) and Cluster 2 (Figure 3b) were extracted from the periodic structure of Zr-MOF-808 to simulate the adsorption states of gas molecules in pores with sizes of 0.48 nm and 1.84 nm, respectively. Then, we deleted one carboxyl group from each of the two saturated Zr atoms on the two clusters to simulate the unsaturated coordination metal sites generated during the synthesis of Zr-MOF-808.

Cluster 1 is a shared vertex of two tetrahedral cages. The core of Cluster 1 consists of six Zr atoms in an octahedral shape, and each Zr atom is connected to two benzene rings by carboxyl groups. The central region, which is wrapped in three benzene rings, forms the 0.48 nm pore of the tetrahedral cage. Upon deleting one of the carboxyl groups connected to the benzene ring and two Zr atoms, we analyzed the adsorption characteristics of gas molecules in the 0.48 nm pores. Cluster 2 is an octahedral cage comprising six Zr atoms and adjacent carboxyl groups. Upon deleting a carboxyl group near the 1.84 nm pore, the adsorption characteristics of gas molecules in the macropores of Zr-MOF-808 were simulated. The optimized clusters and molecular gas models are shown in Figure 4.

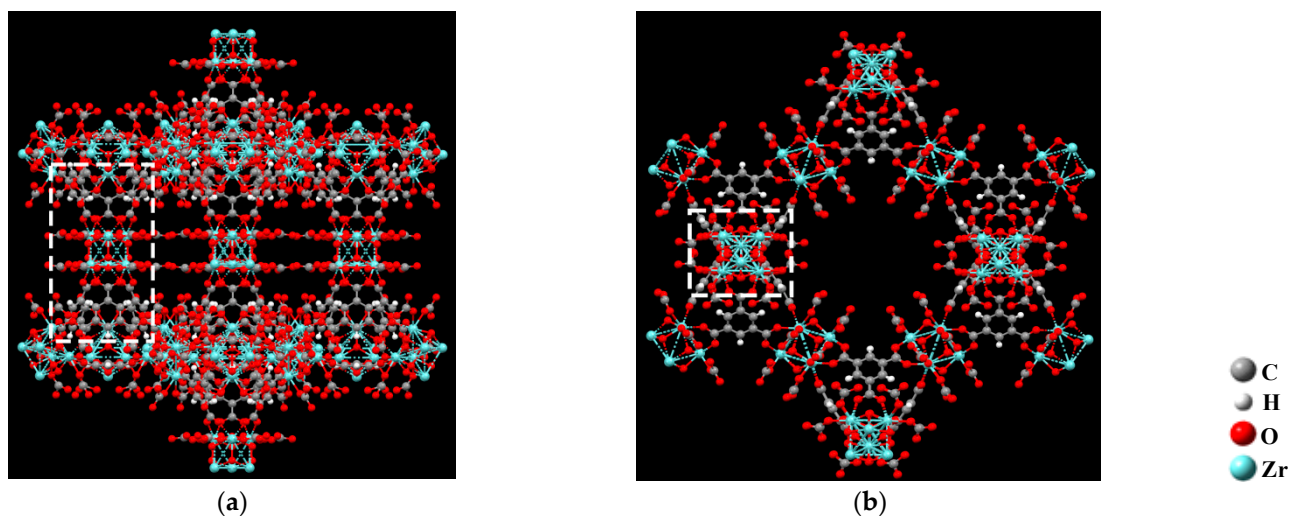


Figure 3. Two pore sizes of Zr-MOF-808: (a) Cluster 1; (b) Cluster 2.

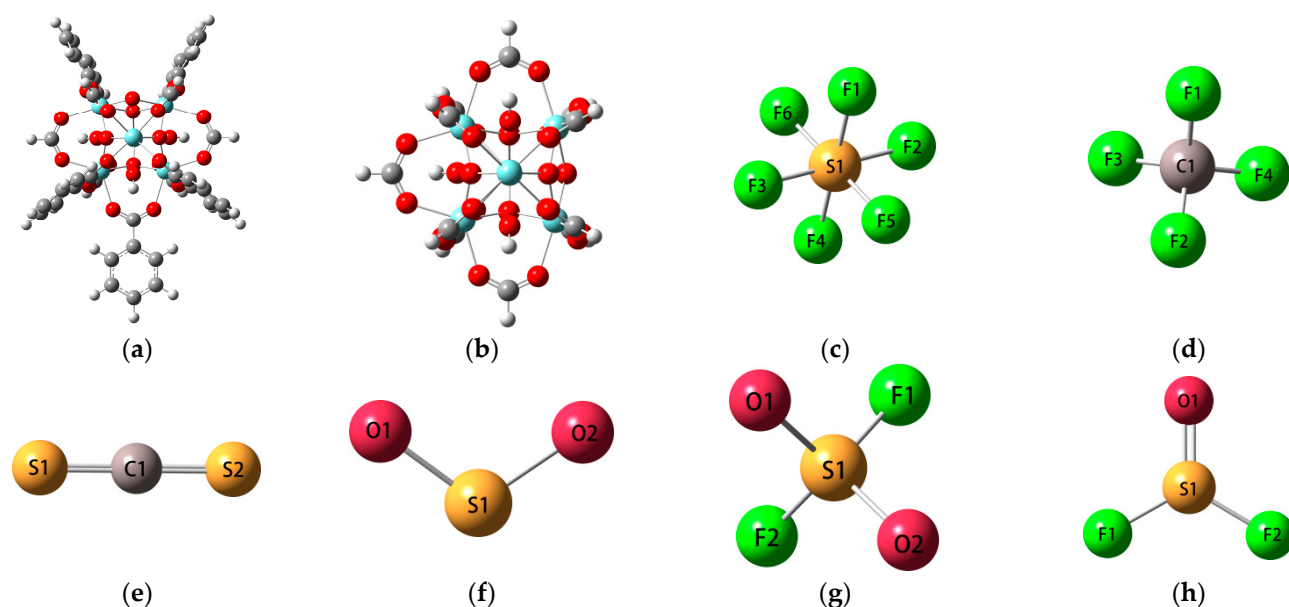


Figure 4. Structure optimized model of Cluster1, Cluster2, and gases: (a) Cluster 1; (b) Cluster 2; (c) SF₆; (d) CF₄; (e) CS₂; (f) SO₂; (g) SO₂F₂; (h) SOF₂.

We calculate the binding energy ($E_{binding}$) to reflect the changes in the total energy of each system during the adsorption process, which can reflect the strength of the adsorption interaction between the gas molecule and the Zr-MOF-808 cluster.

$$E_{binding} = E_{MOF-gas} + E_{BSSE} - E_{MOF} - E_{gas}, \quad (1)$$

In Equation (1), $E_{MOF-gas}$ is the total energy of the system after Zr-MOF-808 adsorbed the gas molecules, and E_{BSSE} is the corrected value of the basis-set superposition error (BSSE) throughout the counterpoise method proposed by Boys and Bernardi [49]. E_{MOF} is the total energy of the Zr-MOF-808 clusters before adsorption, and E_{gas} is the total energy of the gas molecules before adsorption.

We describe the gain and loss of electrons in the gas molecules and the Zr-MOF-808 cluster during the adsorption process by the transfer charge of the gas molecules.

$$\Delta Q = Q_1 - Q_2, \quad (2)$$

In Equation (2), ΔQ represents the charge transfer of the system, with Q_1 signifying the charge of the gas molecules post-adsorption and Q_2 indicating the charge of the gas molecules prior to adsorption. A positive ΔQ infers that the gas molecule has gained electrons, while a negative ΔQ suggests electron loss by the gas molecule.

The definition of the adsorption distance lies in the gap between a gas molecule and a Zr-MOF-808 adsorption site.

To obtain the density-of-states (DOS) curve, a Gaussian function was employed to broaden the discrete orbital occupation diagram. Further analysis of the gases' chemical adsorption on Zr-MOF-808 was carried out using the total density of states, the gas density of states, and the local density of states.

3. Results and Discussion

The adsorption point calculations in this study were conducted by bringing six gas molecules perpendicularly close to the unsaturated Zr atoms in the Zr-MOF-808 clusters. Once the calculations converged, the binding energy and charge transfer were extracted, and the adsorption distance, bond length, and bond angle changes of the gas molecules were quantified using GaussView. The discrete orbital occupation information was imported into Multiwfn, broadened by Gaussian functions, and then plotted into continuous DOS curves to analyze the hybridization phenomena between atoms.

3.1. Parameters of Adsorption

The adsorption energies, charge transfer, and adsorption distance in the adsorption processes of the six gas molecules—SF₆, CF₄, CS₂, SO₂, SO₂F₂, and SOF₂—on Zr-MOF-808 clusters are listed in Table 1.

Table 1. Adsorption energies, charge transfer, and adsorption distance.

Cluster	Gas	SF ₆	CF ₄	CS ₂	SO ₂	SO ₂ F ₂	SOF ₂
Cluster 1	Adsorption energy (eV)	−0.218	−0.223	−0.354	−0.544	−0.526	−0.399
	transfer charge (e)	0.150	0.145	0.147	0.321	0.299	0.282
	Adsorption distance (Å)	3.083	3.077	3.235	2.223	2.562	2.532
Cluster 2	Adsorption energy (eV)	−0.225	−0.218	−0.338	−0.599	−0.518	−0.451
	transfer charge (e)	0.150	0.145	0.147	0.321	0.299	0.282
	Adsorption distance (Å)	3.083	3.077	3.235	2.223	2.562	2.532

According to the adsorption energy calculated with Formula (1) in this study, the relationships between the adsorption capacities of Cluster 1 and Cluster 2 for each gas were SO₂ > SO₂F₂ > SOF₂ > CS₂ > SF₆ > CF₄. It can be seen from the slight difference in the adsorption energy values that the benzene ring had little effect on the adsorption energy, which is consistent with the results reported in the literature [50].

It can be seen in Formula (2) that the gas molecules lost electrons during the adsorption process, and Clusters 1 and 2 gained electrons. The gas transfer charge for Cluster 1 and 2 were the same throughout the adsorption process. After adsorption, the distance between gas molecules and metal sites in each system was also the same. Based on the comprehensive adsorption energy values, it could be speculated that when there were unsaturated Zr coordination atoms in the pores, the gas molecules were less affected by adsorption with different pore sizes.

Therefore, in the following, we only use Cluster 1 as the adsorption substrate to show the IGMH model and to analyze the changes in the bond length, bond angle, density of states, and frontier molecular orbital of gas molecules.

3.2. IGMH Model of the System after Adsorption

In recent years, the independent gradient model (IGM) method has become more and more popular in the visual analysis of intramolecular and intermolecular interactions. However, when IGM maps are used to study weak interactions on graphs, the isosurfaces

are usually too convex, which may lead to errors in the analysis conclusions. An IGM based on the Hirshfeld molecular density partition (IGMH) was proposed by Tian, L. et al. to replace the free-state atomic density involved in the IGM method [51].

We used the $\text{sign}(\lambda^2)\rho$ function to project the type and intensity of interaction onto the isosurfaces of δg , δg_{inter} , and δg_{intra} with different colors. It can be seen from the colors of the isosurfaces in Figure 5a–c that the F atoms and S atoms in the CF_4 , SF_6 , and CS_2 gases had weak interactions with the Zr atoms in the adsorbed substrate. There was a strong interaction between O atoms in SO_2 , SO_2F_2 , and SOF_2 gases and the Zr atoms in the adsorbed substrate (Figure 5d–f).

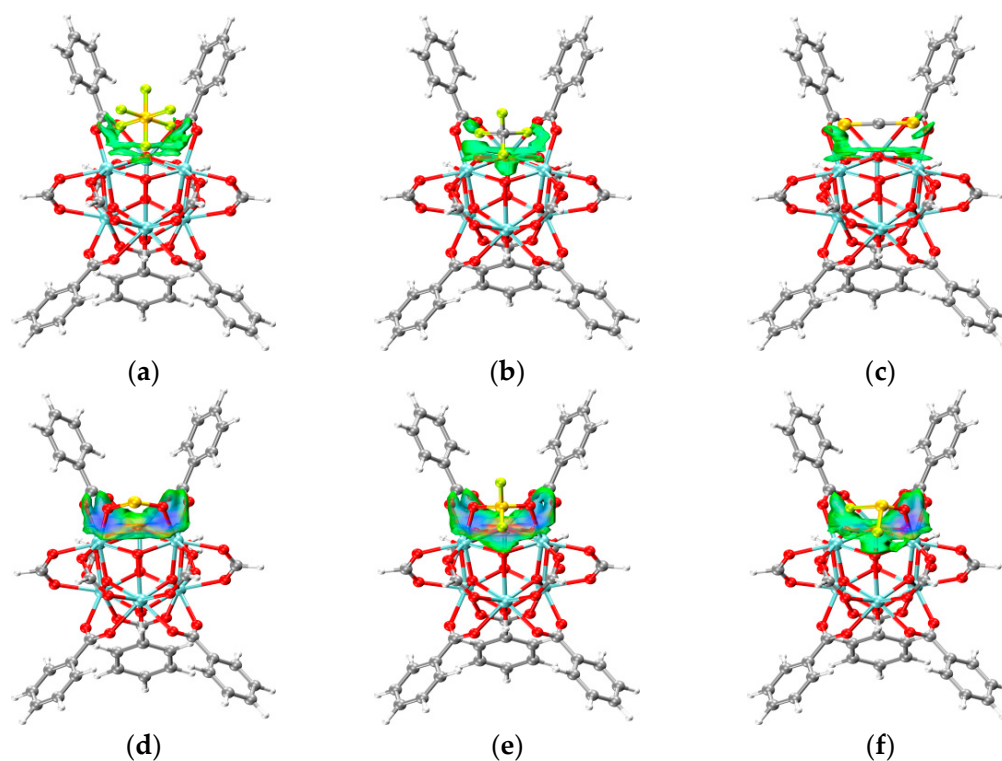


Figure 5. IGMH model of gas molecules on Zr-MOF-808 cluster: (a) SF_6 ; (b) CF_4 ; (c) CS_2 ; (d) SO_2 ; (e) SO_2F_2 ; (f) SOF_2 .

3.3. Changes in Bond Length and Bond Angle after the Adsorption of Gas Molecules

The changes in bond length and angle of the SF_6 , CF_4 , CS_2 , SO_2 , SO_2F_2 , and SOF_2 gas molecules before and after adsorption are shown in the Supplementary Material (Tables S1–S12).

There were slight changes in the bond lengths and bond angles of the six gas molecules due to adsorption, and the obvious changes in the bond angle (the atomic numbers are shown in Figure 4c–h) are the following: The F(3)–S(1)–F(2) bond angle in SF_6 decreased by 1.2° ; the O(2)–S(1)–O(1) bond angle in SO_2 decreased by 1.1° ; the O(1)–S(1)–F(2) and O(2)–S(1)–F(2) bond angles in SO_2F_2 decreased by 2.21° and 2.24° , respectively, while the O(2)–S(1)–O(1) bond angle increased by 2.77° ; the F(2)–S(1)–F(1) and O(1)–S(1)–F(1) bond angles in SOF_2 increased by 1.43° and 1.46° .

The changes in the bond length and bond angle before and after the adsorption of these six gas molecules, together with the adsorption energy, adsorption distance, transfer charge, and IGMH model of each system after adsorption, strongly proved that the gas molecules and the adsorption substrate had different interactions.

3.4. The Changes in the Orbital Occupation of Each System before and after Gas Adsorption

Pomogaeva, A.V. et al. furnished a comprehensive account of how to transport the orbital occupation computation outcomes from Gaussian 16 software into the wave function

analysis tool Multiwfn, in order to acquire discrete orbital occupation data at varying energy levels. Upon broadening with a Gaussian function, a continuous density of states (DOS) map can be generated [52].

This method is applied in this paper to analyze the congruence of the DOS curves of Zr's 5s and 4d orbitals on Zr-MOF-808 with those of the outer orbitals of the active site atoms of SF₆, CF₄, CS₂, SO₂, SO₂F₂, and SOF₂ gas molecules. This analysis assists in studying the hybridization occurrence between the cluster and gas molecules during the adsorption process.

1. The changes in the DOS of Zr-MOF-808 Cluster 1 after SF₆ adsorption are shown in Figure 6a–c.

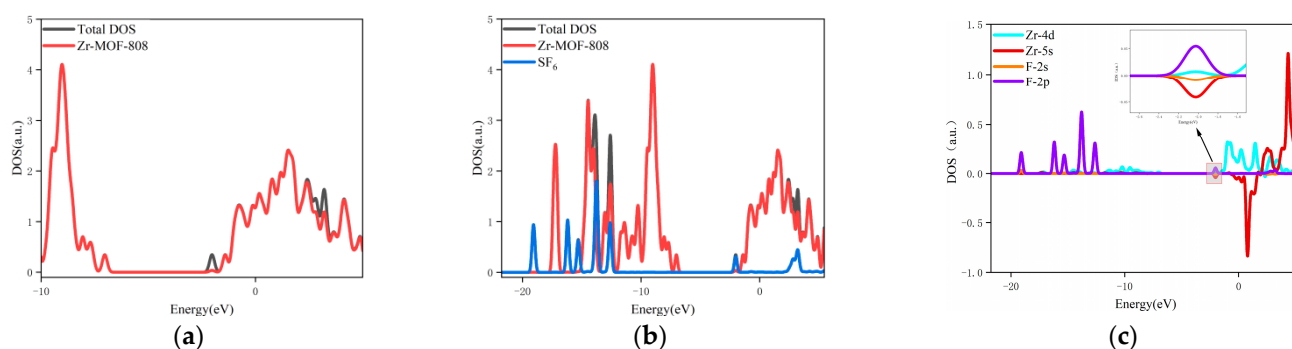


Figure 6. DOS changes of Cluster 1 after adsorbing SF₆: (a) TDOS curves of Zr-MOF-808 Cluster 1 before and after gas adsorption; (b) The contribution of Cluster 1 and SF₆ molecules in the TDOS curve after adsorption; (c) The outer electron PDOS curves of Zr and F atoms.

The changes in the DOS of Zr-MOF-808 cluster 1 after SF₆ adsorption are shown in Figure 6a–c. Compared to the cluster before SF₆ adsorption, a new DOS peak appears near the -2.02 eV position of the TDOS curve after gas adsorption, and the curve shows minor changes near energy positions such as 2.80 eV and 3.20 eV (Figure 6a). As combined with Figure 6b, it is known that the aforementioned changes in the TDOS curve are contributed by the SF₆ molecules adsorbed by the cluster. Further comparison analysis of the PDOS curves (Figure 6c) concludes that the PDOS curves of the 4d orbitals of Zr atoms overlap with those of 2p orbitals of F atoms in $-2.36\sim-1.70$ eV section. This indicates that there is an orbital hybridization effect between Zr atoms and F atoms, which further reveals the chemical adsorption effect of cluster 1 on SF₆.

2. The changes in the DOS of Zr-MOF-808 Cluster 1 after CF₄ adsorption are shown in Figure 7a–c.

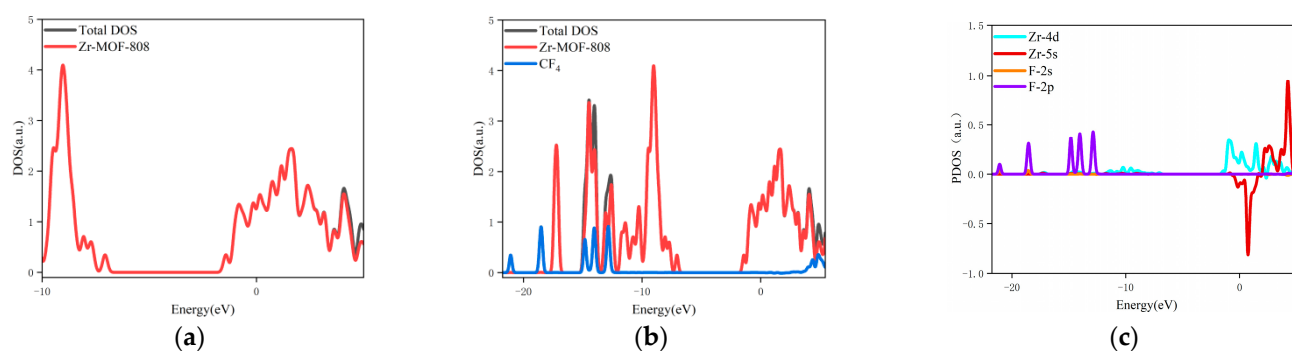


Figure 7. DOS changes of Cluster 1 after adsorbing CF₄: (a) TDOS curves of Zr-MOF-808 Cluster 1 before and after gas adsorption; (b) The contribution of Cluster 1 and CF₄ molecules in the TDOS curve after adsorption; (c) The outer electron PDOS curves of Zr and F atoms.

Compared to the cluster before CF_4 adsorption, a new DOS peak appears near the -2.02 eV position of the TDOS curve after gas adsorption, and the curve shows very minor changes at energy positions of 4.08 eV and 4.88 eV (Figure 7a). As combined with Figure 7(b), it is known that the aforementioned changes in the TDOS curve are contributed by the CF_4 molecules adsorbed by the cluster. After further comparison analysis of the PDOS curves of the outer electrons of the atoms at the interaction points of the cluster and CF_4 molecules (Figure 7c), it can be concluded that there is no overlap in the PDOS curves of the outer electron orbits of Zr atoms and F atoms in $21.76\sim 5.44$ eV section. This indicates that there is no orbital hybridization effect between Zr atoms and F atoms, which further reveals that there is basically no chemical adsorption effect of Cluster 1 on CF_4 .

3. The changes in the DOS of Zr-MOF-808 Cluster 1 after CS_2 adsorption are shown in Figure 8a–c.

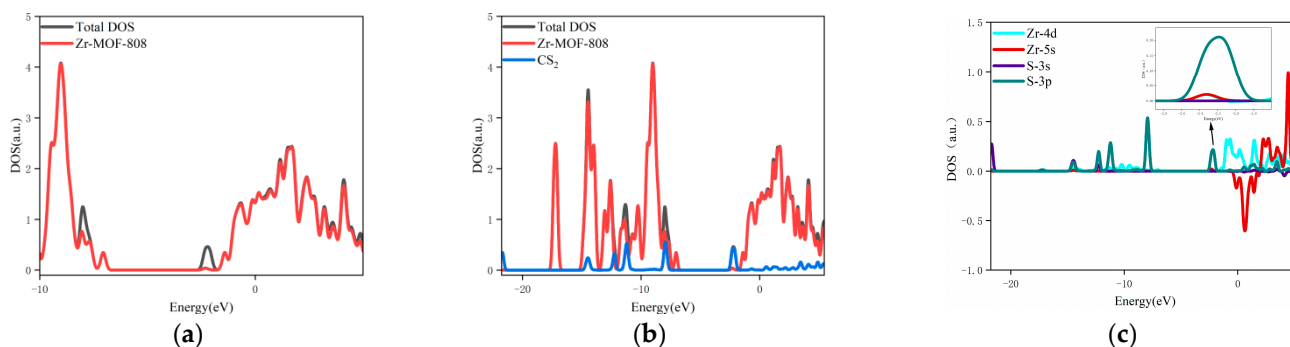


Figure 8. DOS changes of Cluster 1 after adsorbing CS_2 : (a) TDOS curves of Zr-MOF-808 Cluster 1 before and after gas adsorption; (b) The contribution of Cluster 1 and CS_2 molecules in the TDOS curve after adsorption; (c) The outer electron PDOS curves of Zr and S atoms.

Compared to the cluster before CS_2 adsorption, a new DOS peak appears near the -2.32 eV position of the TDOS curve after gas adsorption, and the curve shows minor changes at energy positions such as -8.00 eV, -2.32 eV, and -0.65 eV (Figure 8a). As combined with Figure 8b, it is known that the aforementioned changes in the TDOS curve are contributed by the CS_2 molecules adsorbed by the cluster. After further comparison analysis of the PDOS curves of the outer electrons of the atoms at the interaction points of the cluster and CS_2 molecules (Figure 8c), it can be concluded that the PDOS curves of the 5s and 4d orbitals of Zr atoms overlap with the ones of 3p orbitals of S atoms in $-2.62\sim -2.10$ eV section. This indicates that there is an orbital hybridization effect between Zr atoms and S atoms, which further reveals the chemical adsorption effect of Cluster 1 on CS_2 .

4. The changes in the DOS of Zr-MOF-808 Cluster 1 after SO_2 adsorption are shown in Figure 9a–c.

Compared to the cluster before SO_2 adsorption, a new DOS peak appears near the -4.80 eV position of the TDOS curve after gas adsorption, and the curve shows minor changes at energy positions such as -4.80 eV, 0.35 eV, and 2.79 eV (Figure 9a). As combined with Figure 9b, it is known that the aforementioned changes in the TDOS curve are contributed by the SO_2 molecules adsorbed by the cluster. After further comparison analysis of the PDOS curves of the outer electrons of the atoms at the interaction points of the cluster and SO_2 molecules (Figure 9c), it can be concluded that the PDOS curves of the 5s and 4d orbitals of Zr atoms overlap with the ones of 2p orbitals of O atoms in $-5.16\sim -4.45$ eV section. This indicates that there is an orbital hybridization effect between Zr atoms and O atoms, which further reveals the chemical adsorption effect of Cluster 1 on SO_2 .

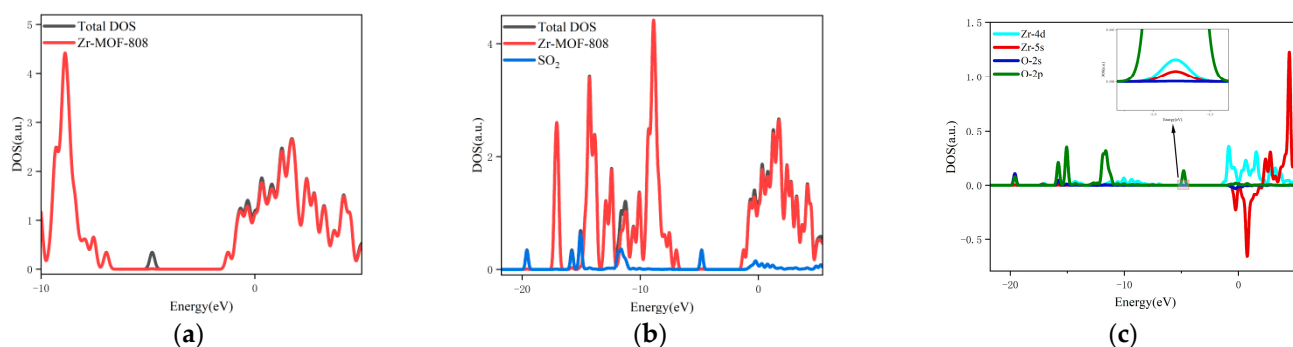


Figure 9. DOS changes of Cluster 1 after adsorbing SO₂: (a) TDOS curves of Zr-MOF-808 Cluster 1 before and after gas adsorption; (b) The contribution of Cluster 1 and SO₂ molecules in the TDOS curve after adsorption; (c) The outer electron PDOS curves of Zr and O atoms.

5. The changes in the DOS of Zr-MOF-808 Cluster 1 after SO₂F₂ adsorption are shown in Figure 10a–c.

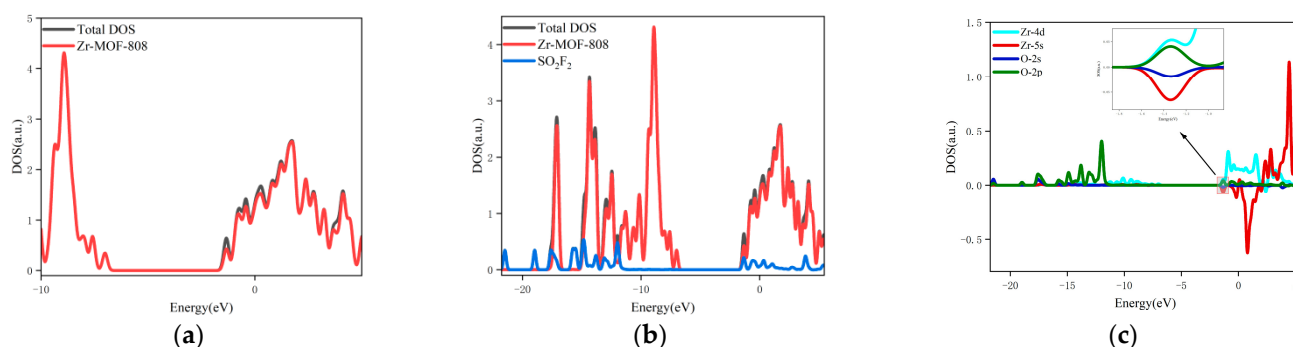


Figure 10. DOS changes of Cluster 1 after adsorbing SO₂F₂: (a) TDOS curves of Zr-MOF-808 Cluster 1 before and after gas adsorption; (b) The contribution of cluster 1 and SO₂F₂ molecules in the TDOS curve after adsorption; (c) The outer electron PDOS curves of Zr and O atoms.

Compared to the cluster before SO₂F₂ adsorption, no new DOS peak appears in the TDOS curve after gas adsorption, but the curve shows minor changes near energy positions such as -1.33 eV, 0.28 eV, and 1.73 eV (Figure 10a). As combined with Figure 10b, it is known that the aforementioned changes in the TDOS curve are contributed by the SO₂F₂ molecules adsorbed by the cluster. After further comparison analysis of the PDOS curves of the outer electrons of the atoms at the interaction points of the cluster and SO₂F₂ molecules (Figure 10c), it can be concluded that the DOS curves of the 4d orbitals of Zr atoms overlap with the ones of 2p orbitals of O atoms in $-1.72\sim-1.01$ eV sections. This indicates that there is an orbital hybridization effect between Zr atoms and O atoms, which further reveals the chemical adsorption effect of cluster 1 on SO₂F₂.

6. The changes in the DOS of Zr-MOF-808 Cluster 1 after SOF₂ adsorption are shown in Figure 11a–c.

Compared to the cluster before SOF₂ adsorption, a new DOS peak appears near the -2.33 eV position of the TDOS curve after gas adsorption, and the curve shows minor changes at energy positions such as -2.33 eV, -1.28 eV, and 1.74 eV (Figure 11a). As combined with Figure 11b, it is known that the aforementioned changes in the TDOS curve are contributed by the SOF₂ molecules adsorbed by the cluster. After further comparison analysis of the PDOS curves of the outer electrons of the atoms at the interaction points of the cluster and SOF₂ molecules (Figure 11c), it can be concluded that the DOS curves of the 4d orbitals of Zr atoms overlap with those of 2p orbitals of O atoms and the 2p orbitals of F atoms in the $-2.65\sim-2.01$ eV section. This indicates that there is an orbital

hybridization effect between Zr atoms, O atoms, and F atoms, which further reveals the chemical adsorption effect of Cluster 1 on SOF_2 .

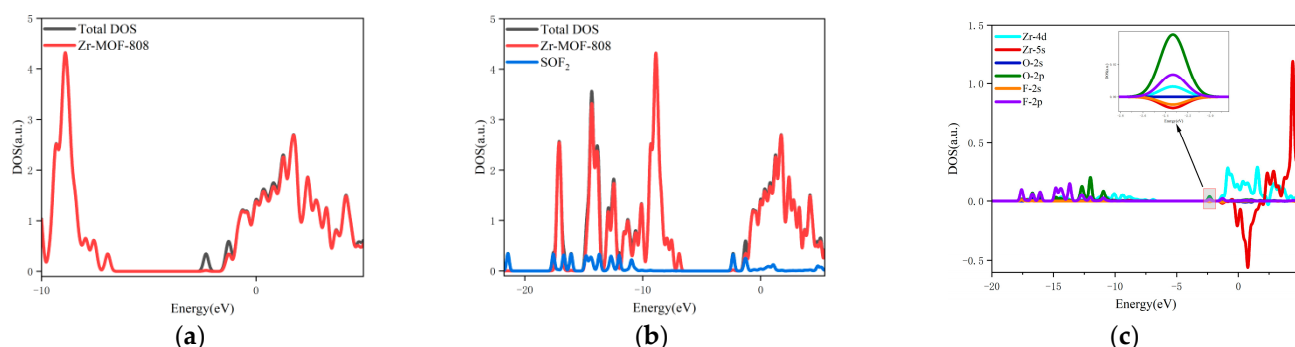


Figure 11. DOS changes of Cluster 1 after adsorbing SOF_2 : (a) TDOS curves of Zr-MOF-808 Cluster 1 before and after gas adsorption; (b) The contribution of Cluster 1 and SOF_2 molecules in the TDOS curve after adsorption; (c) The outer electron PDOS curves of Zr and O atoms.

3.5. Conductivity Analysis

In this section, the change in conductivity of the cluster after gas adsorption is qualitatively analyzed by calculating the HOMO-LUMO gap of the Zr-MOF-808 cluster before and after the adsorption process. Pham, H.Q. and other researchers have concluded that the electronic band structure of the MOFs periodic system can be reflected by the first-principles calculation of the organic linkers in a time-saving and simple way [53]. This conclusion is drawn from the comparison between the calculated values of the HOMO-LUMO gap of the organic linkers in MOFs materials and the experimental band gap values in the literature.

Therefore, we selected Cluster 1, which contains five benzene rings (organic linkers), as the object of analysis. By comparing the changes in the HOMO-LUMO gap before and after the adsorption process in each system, we can speculate on the impact of gas adsorption on the conductivity of Zr-MOF-808 material.

The changes in the HOMO-LUMO gap showed that when the Zr-MOF-808 clusters adsorbed these gases, the conductivity of each system had different degrees of change (as shown in Figure 12). The HOMO-LUMO gap of the CF_4 and SO_2F_2 systems increased, and the conductivity decreased. The conductivity of the other systems increased, and the increase in the SO_2 system was the most obvious.

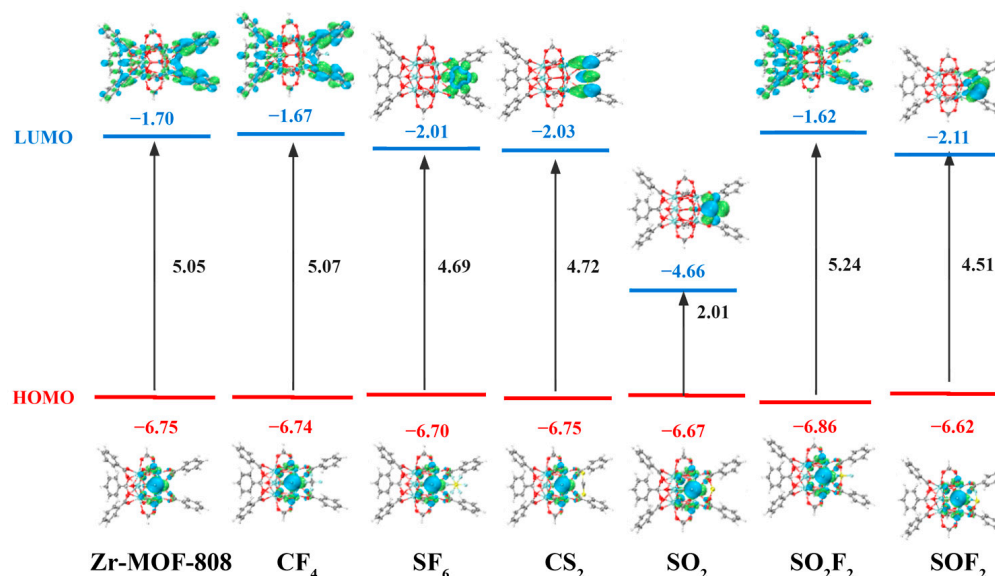


Figure 12. The frontier molecular orbital distributions of Zr-MOF-808 after adsorbing gas molecules.

Thus, it can be postulated that in real-world applications, when a resistance-type gas sensor, having Zr-MOF-808 as the gas-sensitive material, is used to evaluate whether SF₆ has decomposed, the composition of the gas could be analyzed. This can be accomplished by comparing the resistance response variations of the material to the six gases under identical sensor electrode preparation conditions, the same gas flow rate, and an equal measurement temperature.

4. Conclusions

In this study, two clusters of Zr-MOF-808 material and six types of gas molecules (SF₆, CF₄, CS₂, SO₂, SO₂F₂, SOF₂) were modeled by using GaussView software. The adsorption performance of the two Zr-MOF-808 clusters towards gases was simulated using Gaussian16 software, which is based on the principles of quantum chemistry. The main conclusions are as follows:

The Zr-MOF-808 cluster exhibits different adsorption characteristics for each gas molecule. Among the factors affecting the adsorption properties, the unsaturated coordination Zr atom contributes the most, while the benzene ring contributes the least. The clusters perform the same adsorption characteristics for the six gas molecules in the 0.48 nm and 1.84 nm pores of the Zr-MOF-808 structure. In addition, during the adsorption process, Zr atoms in the cluster exhibit electron-gaining behavior, while gas molecules exhibit electron-losing behavior. Furthermore, the adsorption effect causes minor changes in the bond length and bond angle of the gas molecules.

It is concluded from the changes in TDOS and the overlap of PDOS curves that the adsorption of Zr-MOF-808 clusters to CF₄ belongs to the category of physical adsorption, while the adsorption to the other five gases belongs to chemical adsorption.

Changes in the HOMO-LUMO gap indicate that the chemical adsorption of gases by Zr-MOF-808 material leads to changes in the system's conductivity. By comparing the difference in response of this material to the mixed gas in GISs and pure SF₆ gas, it can be determined whether there is a fault inside the equipment.

Therefore, through detailed theoretical calculations in this study, Zr-MOF-808 is expected to become a gas-sensitive material for detecting SF₆ discharge decomposition component gases.

Supplementary Materials: The following supporting information can be downloaded at: <https://www.mdpi.com/article/10.3390/chemosensors11070402/s1>, Table S1: The bond length changes of SF₆ molecules after adsorption; Table S2: The bond angle changes of SF₆ molecules after adsorption; Table S3: The bond length changes of CF₄ molecules after adsorption; Table S4: The bond angle changes of CF₄ molecules after adsorption; Table S5: The bond length changes of CS₂ molecules after adsorption; Table S6: The bond angle changes of CS₂ molecules after adsorption; Table S7: The bond length changes of SO₂ molecules after adsorption; Table S8: The bond angle changes of SO₂ molecules after adsorption; Table S9: The bond length changes of SO₂F₂ molecules after adsorption; Table S10: The bond angle changes of SO₂F₂ molecules after adsorption; Table S11: The bond length changes of SOF₂ molecules after adsorption; Table S12: The bond angle changes of SOF₂ molecules after adsorption.

Author Contributions: Methodology, visualization, formal analysis and writing—original draft, T.L.; supervision, F.L.; validation and investigation, F.L. and B.J.; conceptualization and supervision, T.L. and F.L.; visualization and supervision, F.L.; software and validation, T.L., F.L. and B.J.; supervision, writing—review and editing, F.L. and B.J. All authors have read and agreed to the published version of the manuscript.

Funding: This research was funded by Research and Application of SF₆ Decomposition Component Detection Sensor Technology Based on Modified Nanomaterials, Electric Power Research Institute of Hainan Power Grid Co., Ltd.(730002021030103HH00008).

Institutional Review Board Statement: Not applicable.

Informed Consent Statement: Not applicable.

Data Availability Statement: Not applicable.

Conflicts of Interest: The authors declare no conflict of interest.

References

1. Yaghi, O.M.; Li, H. Hydrothermal Synthesis of a Metal-Organic Framework Containing Large Rectangular Channels. *J. Am. Chem. Soc.* **1995**, *117*, 10401–10402. [[CrossRef](#)]
2. Yaghi, O.M.; O’keeffe, M.; Ockwig, N.W.; Chae, H.K.; Eddaoudi, M.; Kim, J. Reticular synthesis and the design of new materials. *Nature* **2003**, *423*, 705–714. [[CrossRef](#)] [[PubMed](#)]
3. Katayama, Y.; Kalaj, M.; Barcus, K.S.; Cohen, S.M. Self-Assembly of MOF Nanoparticle Monolayer and Free-Standing Multilayers. *J. Am. Chem. Soc.* **2019**, *141*, 20000–20003. [[CrossRef](#)] [[PubMed](#)]
4. Bi, S.; Banda, H.; Chen, M.; Niu, L.; Chen, M.; Wu, T.; Wang, J.; Wang, R.; Feng, J.; Chen, T.; et al. Molecular understanding of charge storage and charging dynamics in supercapacitors with MOF electrodes and ionic liquid electrolytes. *Nat. Mater.* **2020**, *19*, 552–558. [[CrossRef](#)] [[PubMed](#)]
5. Kirchon, A.; Feng, L.; Drake, H.F.; Joseph, E.A.; Zhou, H.-C. From fundamentals to applications: A toolbox for robust and multifunctional MOF materials. *Chem. Soc. Rev.* **2018**, *47*, 8611–8638. [[CrossRef](#)]
6. Hosono, N.; Uemura, T. Development of Functional Materials via Polymer Encapsulation into Meta-Organic Frameworks. *B. Chem. Soc. JPN.* **2021**, *94*, 2139–2148. [[CrossRef](#)]
7. Gonzalez, M.I.; Turkiewicz, A.B.; Darago, L.E.; Oktawiec, J.; Bustillo, K.; Grandjean, F.; Long, G.J.; Long, J.R. Confinement of atomically defined-metal halide sheets in a metal-organic framework. *Nature* **2020**, *577*, 64–68. [[CrossRef](#)]
8. Reddy, R.C.K.; Lin, J.; Chen, Y.; Zeng, C.; Lin, X.; Cai, Y.; Su, C.-Y. Progress of nanostructured metal oxides derived from metal-organic frameworks as anode materials for lithium-ion Batteries. *Coordin. Chem. Rev.* **2020**, *420*, 213434. [[CrossRef](#)]
9. Luo, L.; Lo, W.-S.; Si, X.; Li, H.; Wu, Y.; An, Y.; Zhu, Q.; Chou, L.-Y.; Li, T.; Tsung, C.-K. Directional Engraving within Single-Crystalline Metal-Organic Framework Particles via Oxidative Linker Cleaving. *J. Am. Chem. Soc.* **2019**, *141*, 20365–20370. [[CrossRef](#)]
10. Feng, L.; Yuan, S.; Zhang, L.-L.; Tan, K.; Li, J.-L.; Kirchon, A.; Liu, L.-M.; Zhang, P.; Han, Y.; Chabal, Y.J.; et al. Creating Hierarchical Pores by Controlled Linker Thermolysis in Multivariate Metal-Organic Frameworks. *J. Am. Chem. Soc.* **2018**, *140*, 2363–2372. [[CrossRef](#)]
11. Karadeniz, B.; Žili, D.; Huskic, I.; Germann, L.S.; Fidelli, A.M.; Muratović, S.; Lončarić, I.; Etter, M.; Dinnebier, R.E.; Barišić, D.; et al. Controlling the polymorphism and topology transformation in porphyrinic zirconium metal-organic frameworks via mechanochemistry. *J. Am. Chem. Soc.* **2019**, *141*, 19214–19220. [[CrossRef](#)]
12. Han, Y.; Chen, Y.; Ma, Y.; Bailey, J.; Wang, Z.; Lee, D.; Sheveleva, A.M.; Tuna, F.; McInnes, E.J.L.; Frogley, M.D.; et al. Control of the pore chemistry in metal-organic frameworks for efficient adsorption of benzene and separation of benzene/cyclohexane. *Chem* **2023**, *9*, 739–754. [[CrossRef](#)]
13. Xu, W.; Thapa, K.B.; Ju, Q.; Fang, Z.; Huang, W. Heterogeneous catalysts based on mesoporous metal-organic frameworks. *Coordin. Chem. Rev.* **2018**, *373*, 199–232.
14. Chen, B.; Eddaoudi, M.; Hyde, S.T.; O’Keeffe, M.; Yaghi, O.M. Interwoven metal-organic framework on a periodic minimal surface with extra-large pores. *Science* **2001**, *291*, 1021–1023. [[CrossRef](#)]
15. Wen, Y.; Zhang, J.; Xu, Q.; Wu, X.-T.; Zhu, Q.-L. Pore surface engineering of metal-organic frameworks for heterogeneous catalysis. *Coordin. Chem. Rev.* **2018**, *376*, 248–276. [[CrossRef](#)]
16. Hou, C.-C.; Xu, Q. Metal-Organic Frameworks for Energy. *Adv. Energy Mater.* **2018**, *9*, 1801307. [[CrossRef](#)]
17. Fu, X.-P.; Wang, Y.-L.; Zhang, X.-F.; Krishna, R.; He, C.-T.; Liu, Q.-Y.; Chen, B. Collaborative pore partition and pore surface fluorination within a metal-organic framework for high-performance C₂H₂/CO₂ separation. *Chem. Eng. J.* **2022**, *432*, 134433. [[CrossRef](#)]
18. Tu, T.N.; Nguyen, H.T.D.; Tran, N.T. Tailoring the pore size and shape of the one-dimensional channels in iron-based MOFs for enhancing the methane storage capacity. *Inorg. Chem. Front.* **2019**, *6*, 2441–2447. [[CrossRef](#)]
19. Wang, B.; Zhang, X.; Huang, H.; Zhang, Z.; Yildirim, T.; Zhou, W.; Xiang, S.; Chen, B. A microporous aluminum-based metal-organic framework for high methane, hydrogen, and carbon dioxide storage. *Nano Res.* **2021**, *14*, 507–511. [[CrossRef](#)]
20. Li, J.; Han, X.; Zhang, X.; Sheveleva, A.M.; Cheng, Y.; Tuna, F.; McInnes, E.J.L.; McCormick McPherson, L.J.; Teat, S.J.; Daemen, L.L.; et al. Capture of nitrogen dioxide and conversion to nitric acid in a porous metal-organic framework. *Nat. Chem.* **2019**, *11*, 1085–1090. [[CrossRef](#)]
21. Peng, S.; Bie, B.; Sun, Y.; Liu, M.; Cong, H.; Zhou, W.; Xia, Y.; Tang, H.; Deng, H.; Zhou, X. Metal-organic frameworks for precise inclusion of single-stranded DNA and transfection in immune cells. *Nat. Commun.* **2018**, *9*, 1293. [[CrossRef](#)] [[PubMed](#)]
22. Li, H.; Lv, N.; Xue, L.; Liu, B.; Feng, J.; Ren, X.; Guo, T.; Chen, D.; Stoddart, J.F.; Gref, R.; et al. Composite CD-MOF nanocrystals-containing micro-spheres for sustained drug delivery. *Nanoscale* **2017**, *9*, 7454–7463. [[CrossRef](#)] [[PubMed](#)]
23. Zhao, Y.; Zhuang, S.; Liao, L.; Wang, C.; Xia, N.; Gan, Z.; Gu, W.; Li, J.; Deng, H.; Wu, Z. A Dual Purpose Strategy to Endow Gold Nanoclusters with Both Catalysis Activity and Water Solubility. *J. Am. Chem. Soc.* **2020**, *142*, 973–977. [[CrossRef](#)]
24. Zeng, L.; Wang, Z.; Wang, Y.; Wang, J.; Guo, Y.; Hu, H.; He, X.; Wang, C.; Lin, W. Photo-Activation of Cu Centers in Metal-Organic Frameworks for Selective CO₂ Conversion to Ethanol. *J. Am. Chem. Soc.* **2020**, *142*, 75–79. [[CrossRef](#)]

25. Liang, W.; Bhatt, P.M.; Shkurenko, A.; Adil, K.; Mouchaham, G.; Aggarwal, H.; Mallick, A.; Jamal, A.; Belmabkhout, Y.; Eddaoudi, M. A Tailor-Made Interpenetrated MOF with Exceptional Carbon-Capture Performance from Flue Gas. *Chem* **2019**, *5*, 950–963. [[CrossRef](#)]
26. Gupta, N.K.; López-Olvera, A.; González-Zamora, E.; Martínez-Ahumada, E.; Ibarra, I.A. Sulfur Dioxide Capture in Metal-Organic Frameworks, Metal-Organic Cages, and Porous Organic Cages. *ChemPlusChem* **2022**, *87*, e202200131. [[CrossRef](#)] [[PubMed](#)]
27. Brandt, P.; Nuhnen, A.; Lange, M.; Möllmer, J.; Weingart, O.; Janiak, C. Metal-Organic Frameworks with Potential Application for SO₂ Separation and Flue Gas Desulfurization. *ACS Appl. Mater. Inter.* **2019**, *11*, 17350–17358. [[CrossRef](#)] [[PubMed](#)]
28. Belmabkhout, Y.; Bhatt, P.M.; Adil, K.; Pillai, R.S.; Cadiau, A.; Shkurenko, A.; Maurin, G.; Liu, G.; Koros, W.J.; Eddaoudi, M. Natural gas upgrading using a fluorinated MOF with tuned H₂S and CO₂ adsorption selectivity. *Nat. Energy* **2018**, *3*, 1059–1066. [[CrossRef](#)]
29. Zhuang, Y.; Hu, X.; Tang, B.; Wang, S.; Cui, A.; Hou, K.; He, Y.; Zhu, L.; Li, W.; Chu, J. Effects of SF₆ decomposition components and concentrations on the discharge faults and insulation defects in GIS equipment. *Sci. Rep.* **2020**, *10*, 15039. [[CrossRef](#)]
30. Cho, Y.S.; Hong, T.Y.; Youn, Y.W.; Sun, J.H.; Lee, S.-H. Study on the Correlation between Partial Discharge Energy and SF₆ Decomposition Gas Generation. *Energies* **2020**, *13*, 4655. [[CrossRef](#)]
31. Zeng, F.; Lei, Z.; Yang, X.; Tang, J.; Yao, Q.; Miao, Y. Evaluating DC Partial Discharge with SF₆ Decomposition Characteristics. *IEEE Trans. Power Deliv.* **2019**, *34*, 1383–1392. [[CrossRef](#)]
32. Rao, X.; Tang, J.; Zeng, F.; Li, D.; Xia, X.; Su, Y.; Lu, Y. Mechanism of Trace O₂ on SF₆ Characteristic Decomposed Components Under Spark Discharge. *Plasma Chem. Plasma Process.* **2020**, *40*, 469–481. [[CrossRef](#)]
33. Liu, M. Decomposing Mechanism of SF₆ under Positive DC Partial Discharge in the Presence of Trace H₂O. *ACS Omega* **2020**, *5*, 13389–13395. [[CrossRef](#)]
34. Tang, J.; Zeng, F.; Zhang, X.; Pan, J.; Yao, Q.; Hou, X.; Tang, Y. Relationship between Decomposition Gas Ratios and Partial Discharge Energy in GIS, and the Influence of Residual Water and Oxygen. *IEEE Trans. Dielectr. Electr. Insul.* **2014**, *21*, 1226–1234. [[CrossRef](#)]
35. Zhang, X.; Tian, S.; Xiao, S.; Huang, Y.; Liu, F. Partial discharge decomposition characteristics of typical defects in the gas chamber of SF₆ insulated ring network cabinet. *IEEE Trans. Dielectr. Electr. Insul.* **2017**, *24*, 1794–1801. [[CrossRef](#)]
36. Beyer, C.; Jenett, H.; Kfocow, D. Influence of Reactive SF_x Gases on Electrode Surfaces After Electrical Discharges under SF₆, Atmosphere. *IEEE Trans. Dielectr. Electr. Insul.* **2000**, *7*, 234–240. [[CrossRef](#)]
37. Ammar, S.M.; Zulkurnain, A.-M.; Rai, N.A. SF₆ Decomposed Component Analysis for Partial Discharge Diagnosis in GIS: A Review. *IEEE Access* **2022**, *10*, 27270–27288.
38. Tang, J.; Yang, X.; Yang, D.; Yao, Q.; Miao, Y.; Zhang, C.; Zeng, F. Using SF₆ Decomposed Component Analysis for the Diagnosis of Partial Discharge Severity Initiated by Free Metal Particle Defect. *Energies* **2017**, *10*, 1119. [[CrossRef](#)]
39. Zeng, F.; Tang, J.; Zhang, X.; Xie, Y.; Yao, Q.; Miao, Y. Reconstructing and extracting information on SF₆ decomposition characteristic components induced by partial overthermal fault in GIE. *IEEE Trans. Dielectr. Electr. Insul.* **2016**, *23*, 183–193. [[CrossRef](#)]
40. Yang, A.; Li, W.; Chu, J.; Wang, D.; Yuan, H.; Zhu, J.; Wang, X.; Rong, M. Enhanced sensing of sulfur hexafluoride decomposition components based on noble-metal-functionalized cerium oxide. *Mater. Design* **2020**, *187*, 08391. [[CrossRef](#)]
41. Wang, Y.; Gui, Y.; Ji, C.; Tang, C.; Zhou, Q.; Li, J.; Zhang, X. Adsorption of SF₆ decomposition components on Pt₃-TiO₂(101) surface: A DFT study. *Appl. Surf. Sci.* **2018**, *459*, 242–248. [[CrossRef](#)]
42. Liu, H.; Wang, F.; Hu, K.; Li, T.; Yan, Y.; Li, J. The adsorption and sensing performances of Ir-modified MoS₂ monolayer toward SF₆ decomposition products: A DFT study. *Nanomaterials* **2021**, *11*, 100. [[CrossRef](#)] [[PubMed](#)]
43. Wang, X.; Liao, Y. Selective detection of SO₂ in SF₆ insulation devices by Rh-doped HfSe₂ monolayer: A first-principles study. *Appl. Phys. A Mater.* **2019**, *125*, 468. [[CrossRef](#)]
44. Chen, D.; Zhang, X.; Tang, J.; Cui, H.; Chen, Z.; Li, Y. Different doping of penta-graphene as adsorbent and gas sensing material for scavenging and detecting SF₆ decomposed species. *Sustain. Mater. Technol.* **2019**, *21*, e00100. [[CrossRef](#)]
45. Chen, D.; Tang, J.; Zhang, X.; Fang, J.; Li, Y.; Zhuo, R. Detecting decompositions of sulfur hexafluoride using reduced graphene oxide decorated with Pt nanoparticles. *J. Phys. D Appl. Phys.* **2018**, *51*, 185304. [[CrossRef](#)]
46. Furukawa, H.; Gándara, F.; Zhang, Y.-B.; Jiang, J.; Queen, W.L.; Hudson, M.R.; Yaghi, O.M. Water Adsorption in Porous Metal–Organic Frameworks and Related Materials. *J. Am. Chem. Soc.* **2014**, *136*, 4369–4381. [[CrossRef](#)]
47. Sciortino, G.; Lihi, N.; Czine, T.; Maréchal, J.-D.; Lledós, A.; Garribba, E. Accurate prediction of vertical electronic transitions of Ni(II) coordination compounds via time dependent density functional theory. *Int. J. Quantum Chem.* **2018**, *118*, e25655. [[CrossRef](#)]
48. Lei, T.X.; Fan, X.Z.; Lv, F.C.; Jiang, B.W. Theoretical Study on Adsorption Behavior of SF₆ Decomposition Components on Mg-MOF-74. *Nanomaterials* **2023**, *13*, 1705. [[CrossRef](#)]
49. Zhang, X.; Wu, J.; Yan, H.; Chen, H.; Mao, W.; Dai, G. Insight into the nature of the noncovalent interactions of furan, pyridine, and pyrazine with AtX. *J. Mol. Model.* **2023**, *29*, 13. [[CrossRef](#)]
50. Li, S.; Zhu, S.; Zhou, Q.; Gui, Y.; Wei, X. Adsorption mechanism of decomposition gas of SF₆ circuit breaker on MOF-505 analogue. *Vacuum* **2021**, *183*, 109816. [[CrossRef](#)]
51. Tian, L.; Qinxue, C. Independent gradient model based on Hirshfeld partition (IGMH): A new method for visual study of interactions in chemical systems. *J. Comput. Chem.* **2022**, *43*, 539–555.

52. Pomogaeva, A.V.; Scheer, M.; Timoshkin, A.Y. Why Do B–P and Al–P Polymers Differ? Structures, Stability, and Electronic Properties of Chain and Ring [H₂PEH₂]_n Oligomers (E=B, Al; n = 1–15). *Chem. Eur. J.* **2018**, *24*, 17046–17054. [[CrossRef](#)] [[PubMed](#)]
53. Pham, H.Q.; Mai, T.; Pham-Tran, N.-N. Engineering of Band Gap in Metal–Organic Frameworks by Functionalizing Organic Linker: A Systematic Density Functional Theory Investigation. *J. Phys. Chem. C* **2014**, *118*, 4567–4577. [[CrossRef](#)]

Disclaimer/Publisher’s Note: The statements, opinions and data contained in all publications are solely those of the individual author(s) and contributor(s) and not of MDPI and/or the editor(s). MDPI and/or the editor(s) disclaim responsibility for any injury to people or property resulting from any ideas, methods, instructions or products referred to in the content.